Supporting Information

Precise Synthesis of Single atom (Mo, W, Nb) Coordinated with Oxygen Functional Groups of Graphene Oxide for Stable and Selective Two-electron Oxygen Reduction in Neutral Media

Chaoran Dong[a], Kug-Seung Lee [b], Yoonjun Cho[c], Shi-Ping Wang[d], Xue-Wen Fan[d], Fu-Quan Bai[d,e], Jong Hyeok Park[c,*], Kan Zhang[a*]

[a] MIIT Key Laboratory of Advanced Display Material and Devices, School of Materials Science and Engineering, Nanjing University of Science and Technology, Nanjing 210094, China

[b] Beamline Division, Pohang Accelerator Laboratory, Pohang, 790-834, Republic of Korea

[c] Department of Chemical and Biomolecular Engineering, Yonsei University, 50 Yonsei-ro, Seodaemun-gu, Seoul 120-749, Republic of Korea

[d] Laboratory of Theoretical and Computational Chemistry, Institute of Theoretical Chemistry and College of Chemistry, Jilin University, Changchun, 130023, China.

[e] Beijing National Laboratory for Molecular Sciences, China

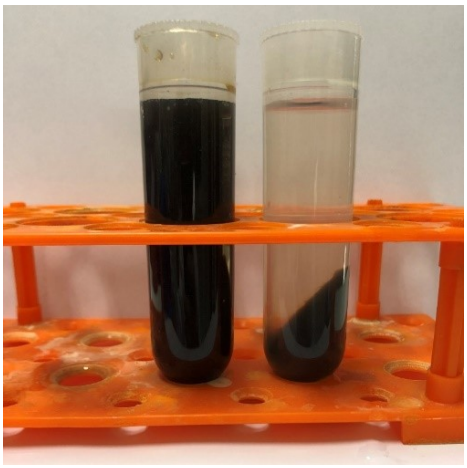

Fig. S1. Optical image of GONS/DMSO and GONS/H_2O solution after centrifugation. Optical image of GONS /DMSO solution (left) and GONS/H_2O (right) solution after centrifugation at 10000 r/min for 20 min, indicating an excellent dispersity of GONS in DMSO.

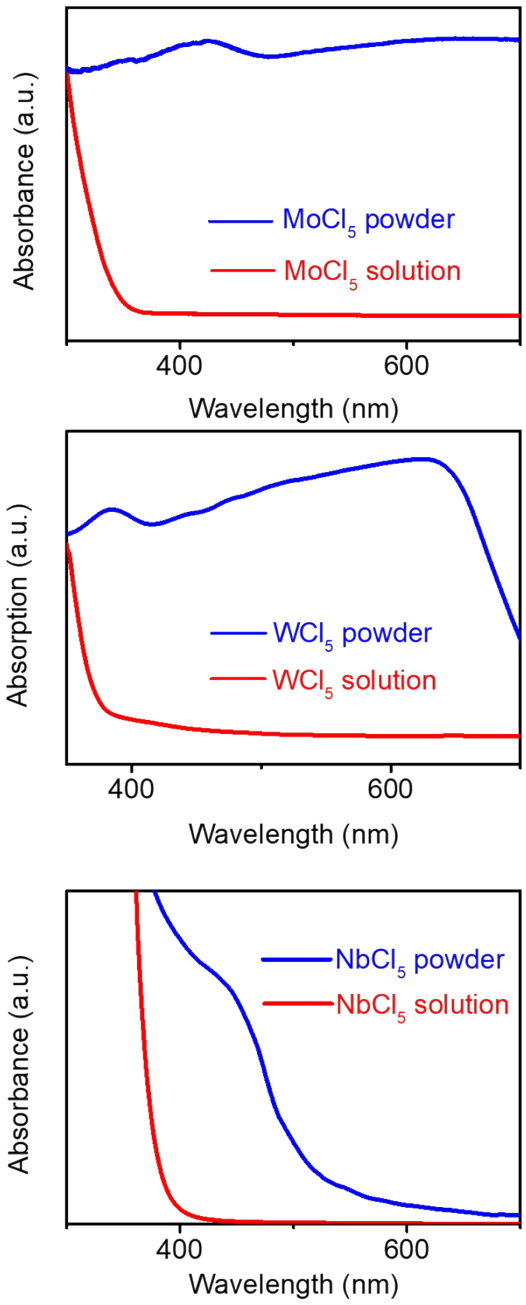

Fig. S2. UV-vis absorption curves of MCl_5 and MCl_5/DMSO solutions. It indicates that the electronic orbitals of the metal are remarkably influenced by DMSO molecular.

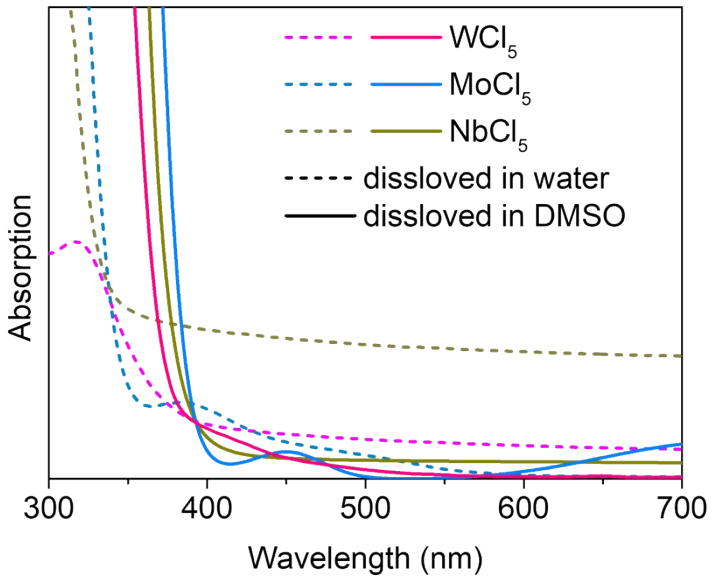

Fig. S3. UV-vis absorption curves of MCl_5/H_2O and MCl_5/DMSO solutions.

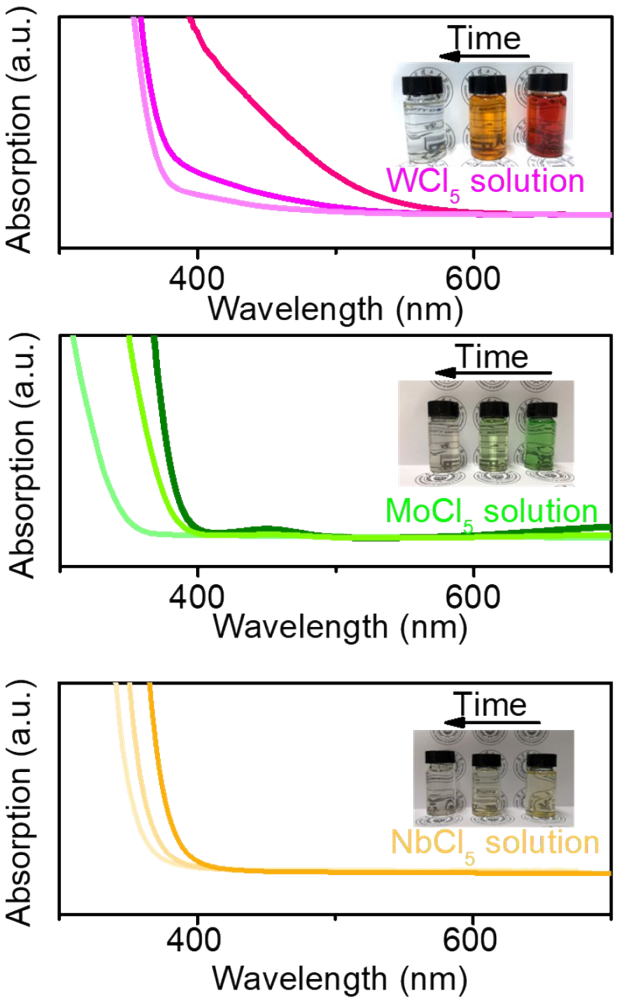

Fig. S4. Time-dependent shifts in the UV-vis absorption curves of MCl_5/DMSO solutions. It indicates that the absorption curves of the metal chloride/DMSO solutions gradually shift towards short wavelengths.

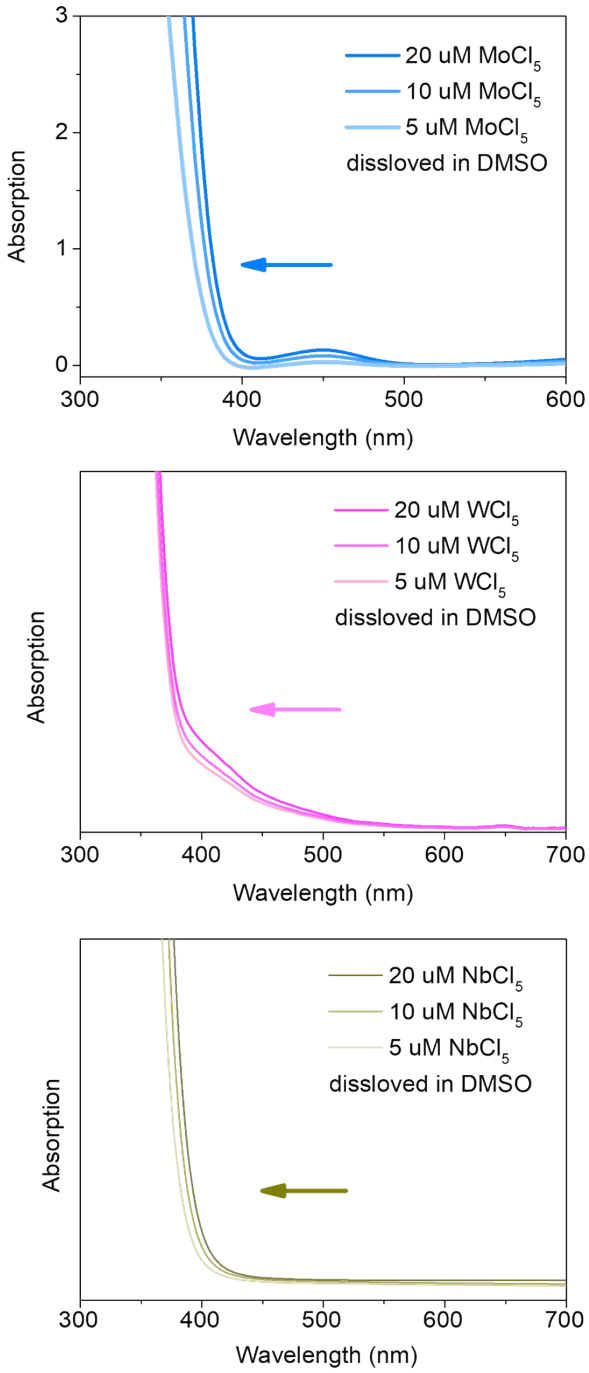

Fig. S5. UV-vis absorption curves of MCl_5/DMSO solutions with different concentration.

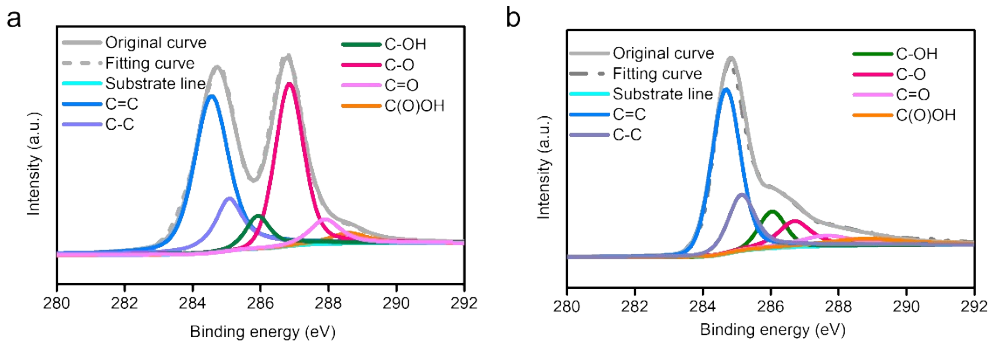

Fig. S6. C 1s X-ray photoelectron spectroscopy (XPS) data for pristine GONS (a) and Mo-SACs/mrG (b). It indicates that GONS could be reduced to a certain extent.

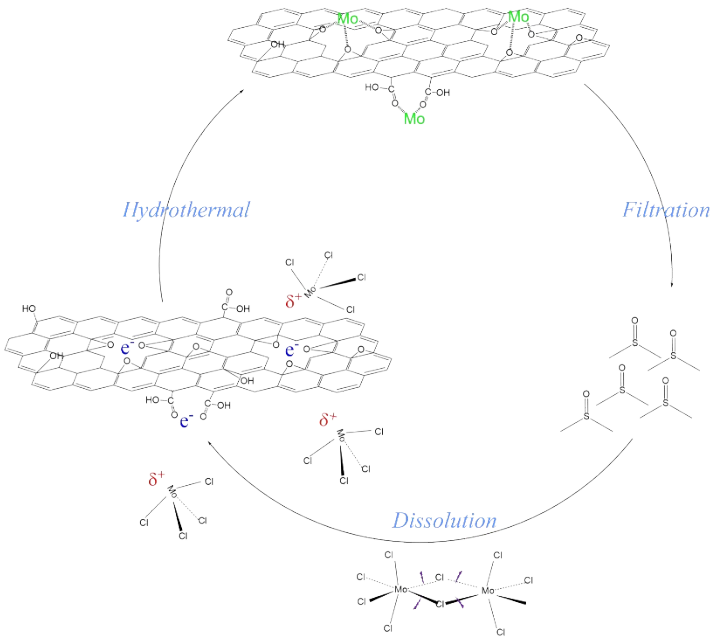

Fig. S7. Mechanism scheme for one-step solvothermal method for M-SACs/mrG (taking Mo for example) with recyclable solvent.

In the “dissolution” stage, the metal chlorides can be dissolved in the aprotic solvent DMSO to dissociate into monomeric pentahalides and leaving behind the positive metal centre (Lewis acid), which is easily attracted by the negative oxygen functional groups (OFGs) (Lewis base) decorated in the carbon matrix. Then, in the “hydrothermal” stage, the metal atom is isolated from aggregation/nucleation under the protection of the DMSO, which provides a stable/inert coordination environment under a modest temperature. Meantime, unlike previous solvothermal methods for the synthesis by using DMSO as the sulfur source, the DMSO solvent used in this method remains stable for not taking part in the chemical reaction (only served as pure solvent) during the hydrothermal reaction for Mo-SACs/mrG. Next, in the “filtration” stage, the chemically inert DMSO solvent can be reused for continuous synthesis.

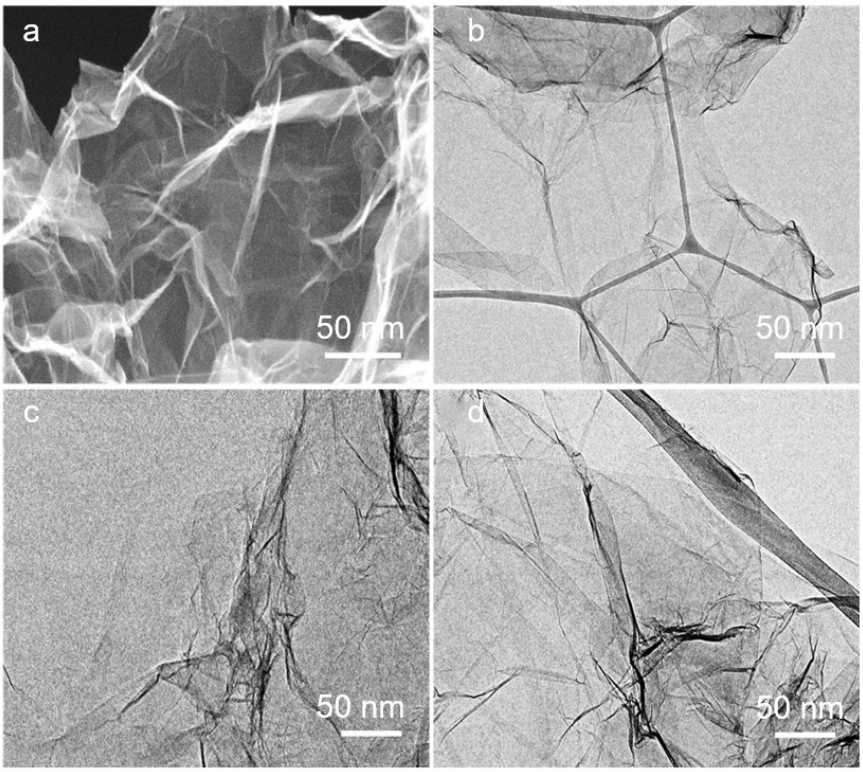

Fig. S8. SEM image of GONS and TEM images of M-SACs/mrG. (a) SEM image of GONS and TEM images of (b) Mo-SACs/mrG; (c) W-SACs/mrG; and (d) Nb-SACs/mrG. The two-dimensional micromorphology with characteristic wrinkles and a smooth surface is well-maintained.

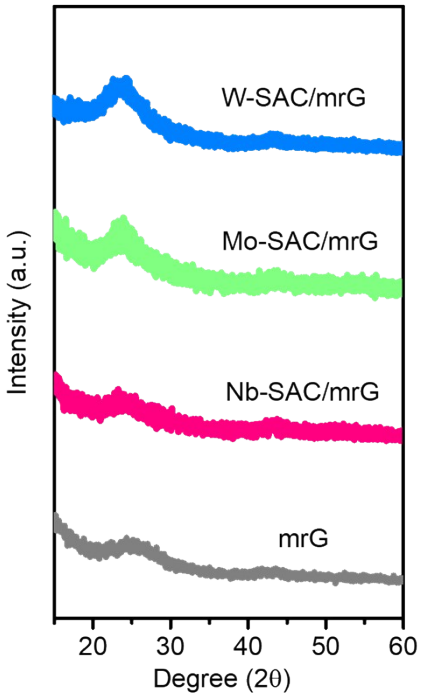

Fig. S9. XRD profiles of mrG and the corresponding M-SACs/mrG materials. It shows that there are no other diffraction peaks related to nanoparticles or other metal species.

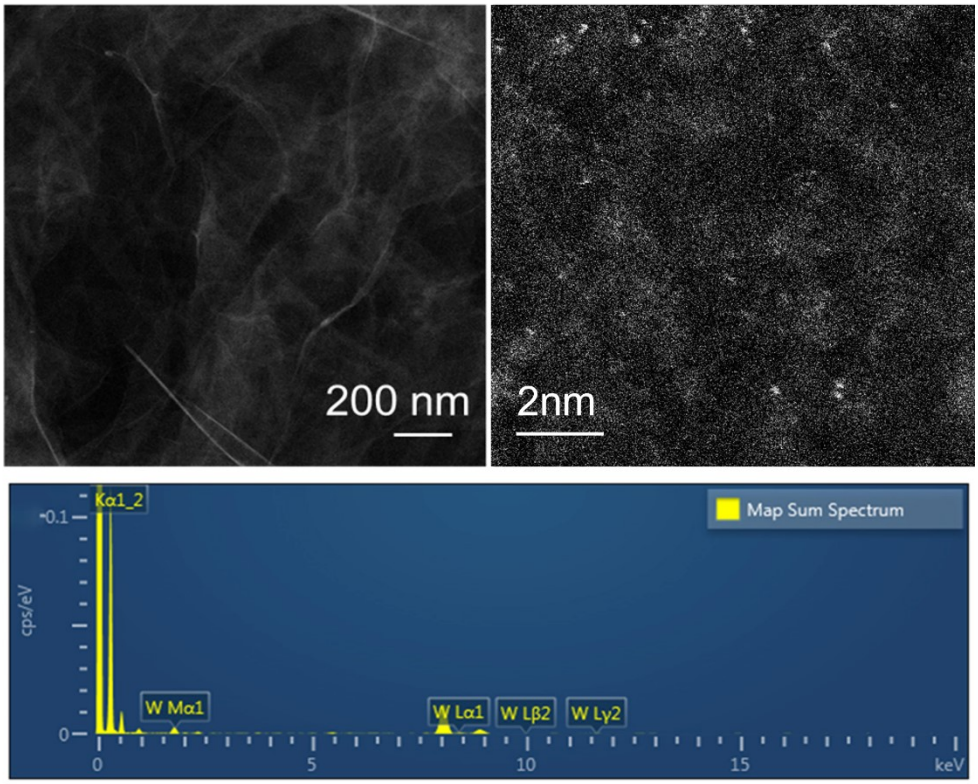

Fig. S10. HAADF-STEM images and element dispersive spectrum of W-SACs/mrG.

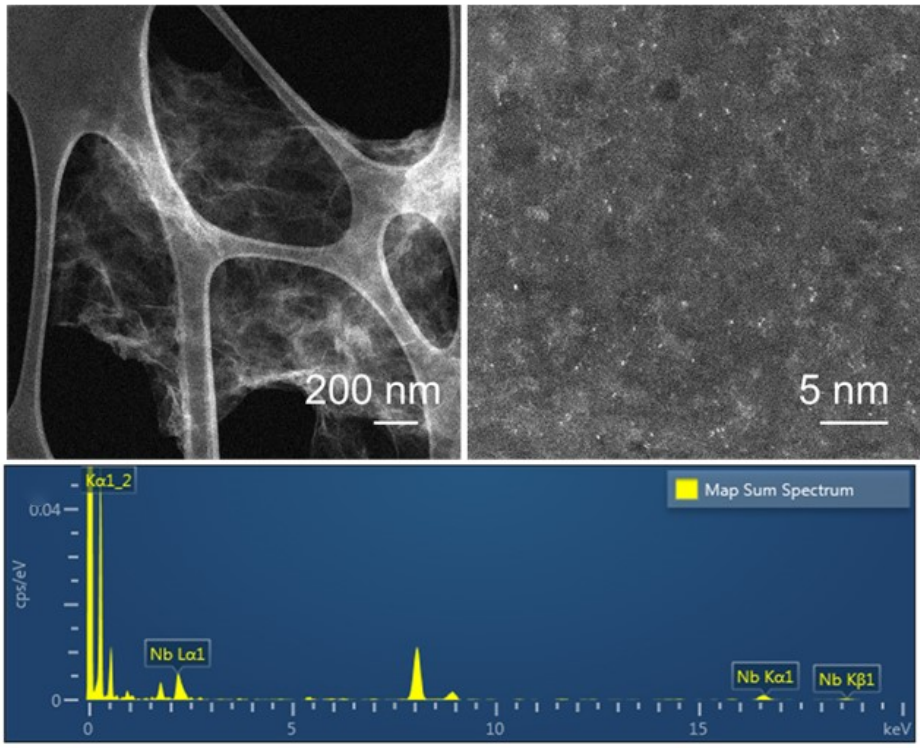

Fig. S11. HAADF-STEM images and element dispersive spectrum of Nb-SACs/mrG.

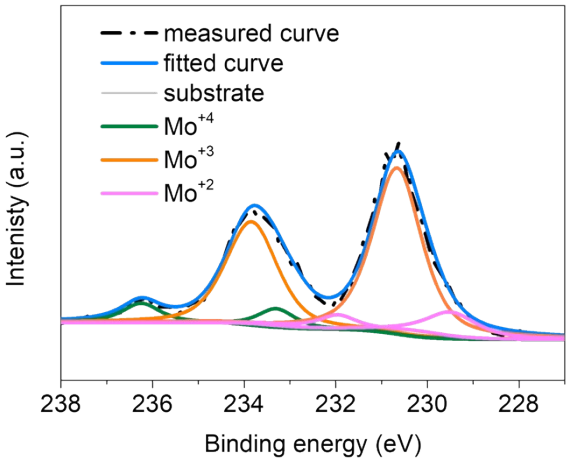

Fig. S12. Mo 3d XPS spectra of Mo-SACs/mrG.

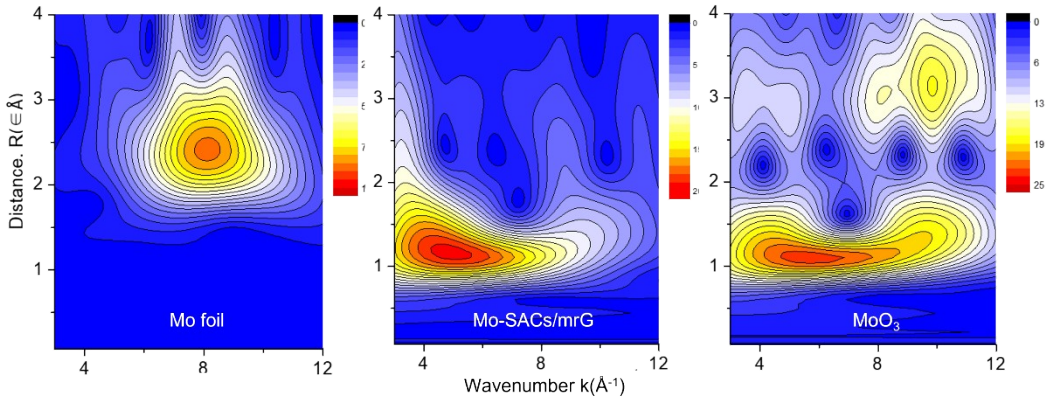

Fig. S13. WT-EXAFS spectrum of Mo foil, Mo-SACs/mrG and MoO_3.

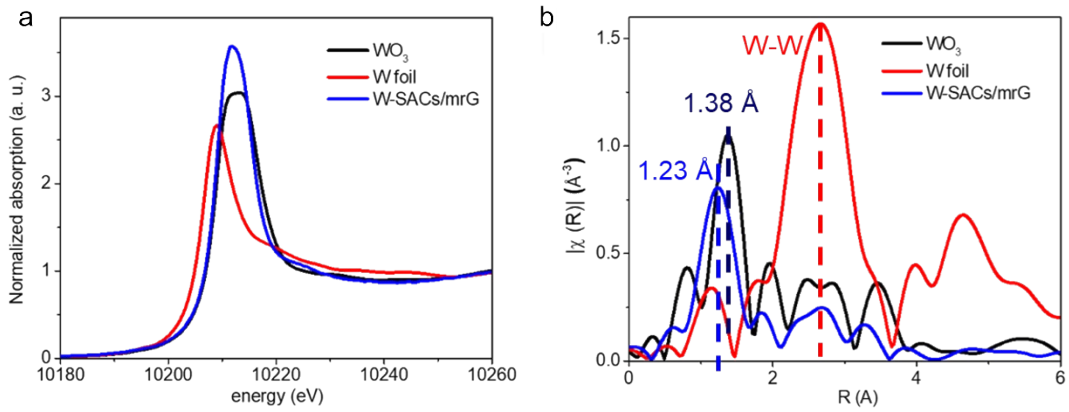

Fig. S14. (a) Normalized XANES spectra at W *L3-edge*. (b) k^3-weighted R-space Fourier transformed spectra from EXAFS. The white line area of W-SACs/mrG is larger than that of WO_3 indicating that the oxidation state of W-SACs/mrG is different than WO_3. The appreciable shift of W-O peak (1.38 Å) for W-SACs/mrG can be detected compared to the WO_3 (1.23 Å), confirming the different W-O environment between W-SACs/mrG and WO_3, while the W-W peak around 2.6 Å may indicate a slight existence of W cluster due to the excessive loading amount of W during the synthesis.

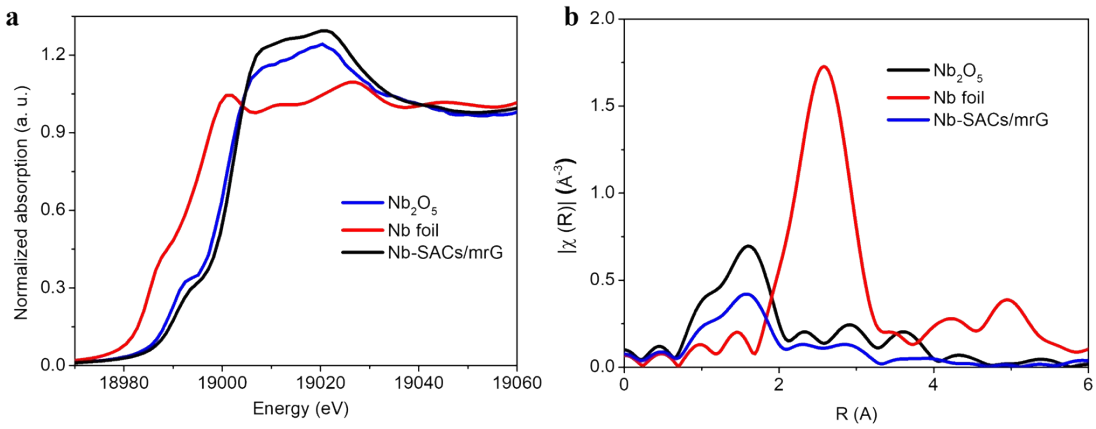

Fig. S15. (a) Normalized XANES spectra at Nb *K*-edge. (b) k^3-weighted R-space Fourier transformed spectra from EXAFS. The intensity of the pre-edge peak of Nb-SACs/mrG is higher and its white line intensity is lower compared to those of Nb_2O_5. The pre-edge absorption is responsible for 1s to 4d transition and the above XANES feature of Nb-SACs/mrG suggests that the site symmetry of Nb for Nb-SACs/mrG is distorted compared to that of Nb_2O_5. The FT-EXAFS of Nb-SACs/mrG does not show Nb-Nb scattering peak at around 2.5Å and 3.6Å indicating Nb-SACs/mrG formed metallic Nb nor Nb oxide phase. Rather, it has only Nb-O scatterings at ~1.5Å, revealing the atomically dispersed Nb atom.

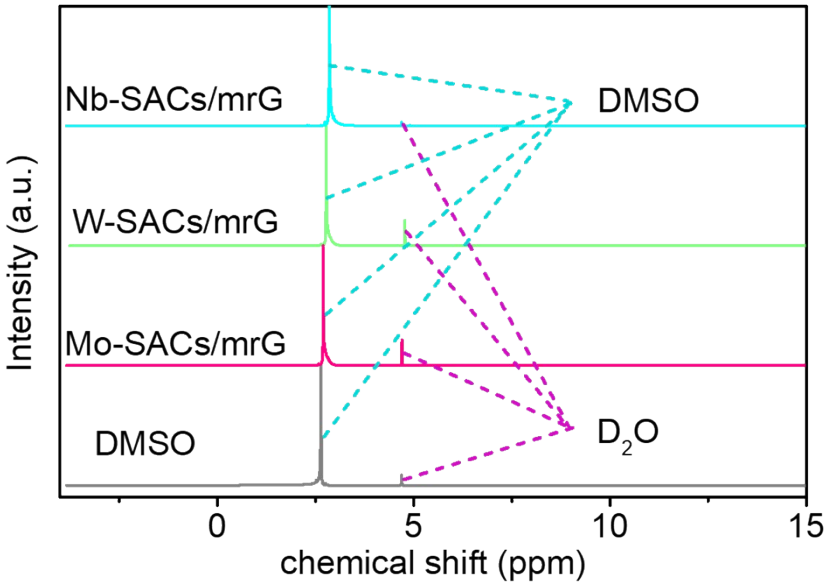

Fig. S16. H1-NMR profiles of the solvent remaining after the solvothermal reaction of each sample. It demonstrates that the DMSO solvent does not participate in the solvothermal reaction or undergo a disproportionation reaction.

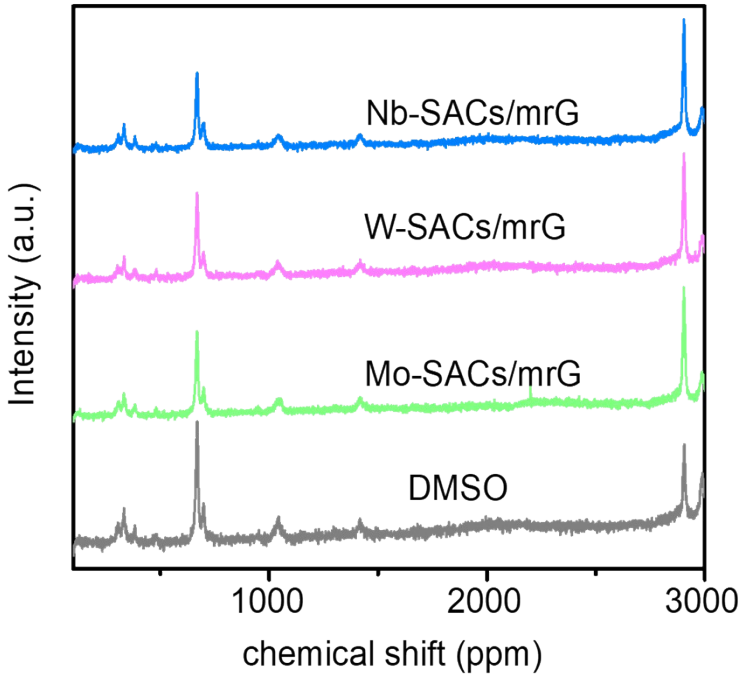

Fig. S17. The Raman spectrum of the solvent remaining after the solvothermal reaction of each sample. It demonstrates that the DMSO solvent does not participate in the solvothermal reaction or undergo a disproportionation reaction.

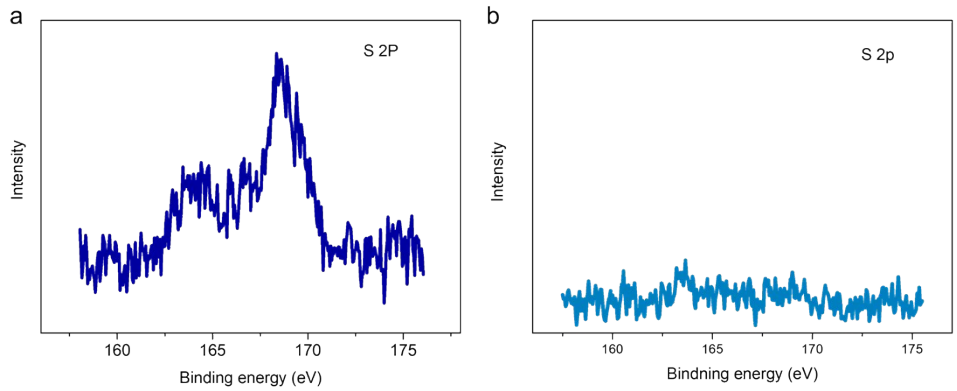

Fig. S18. The XPS spectrum of the S 2p orbitals of (a) Mo-cluster/mrG and (b) Mo-SACs/mrG. An obvious signal of S 2p is observed in Mo-cluster/mrG sample when the reaction temperature is 160 ℃，while barely singal is found in Mo-SACs/mrG sample when reaction temperature is 140 ℃.

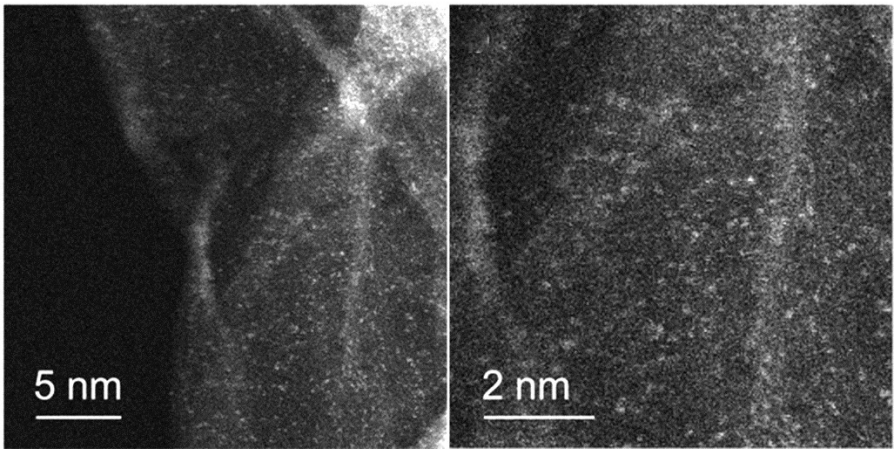

Fig. S19. HAADF-STEM images of Mo-SACs/mrG with reused DMSO solvent. It indicates that DMSO is stable at such a low temperature and can be reused as a low-cost solvent in SAC synthesis.

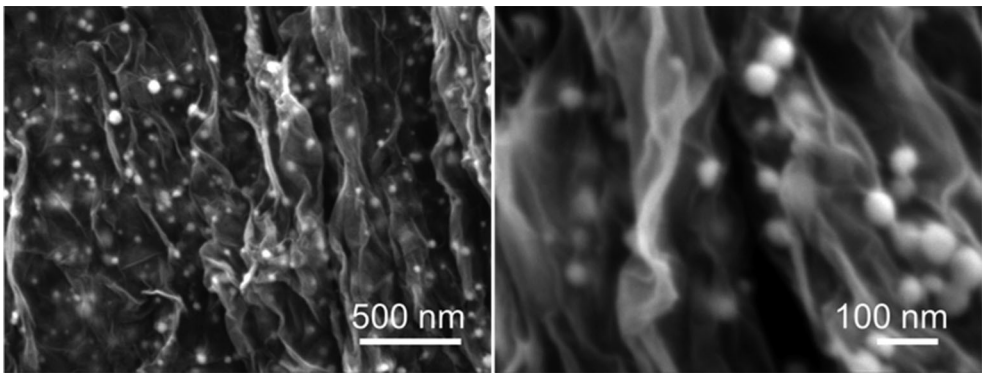

Fig. S20. SEM images of Au-mrG synthesized by the same method.

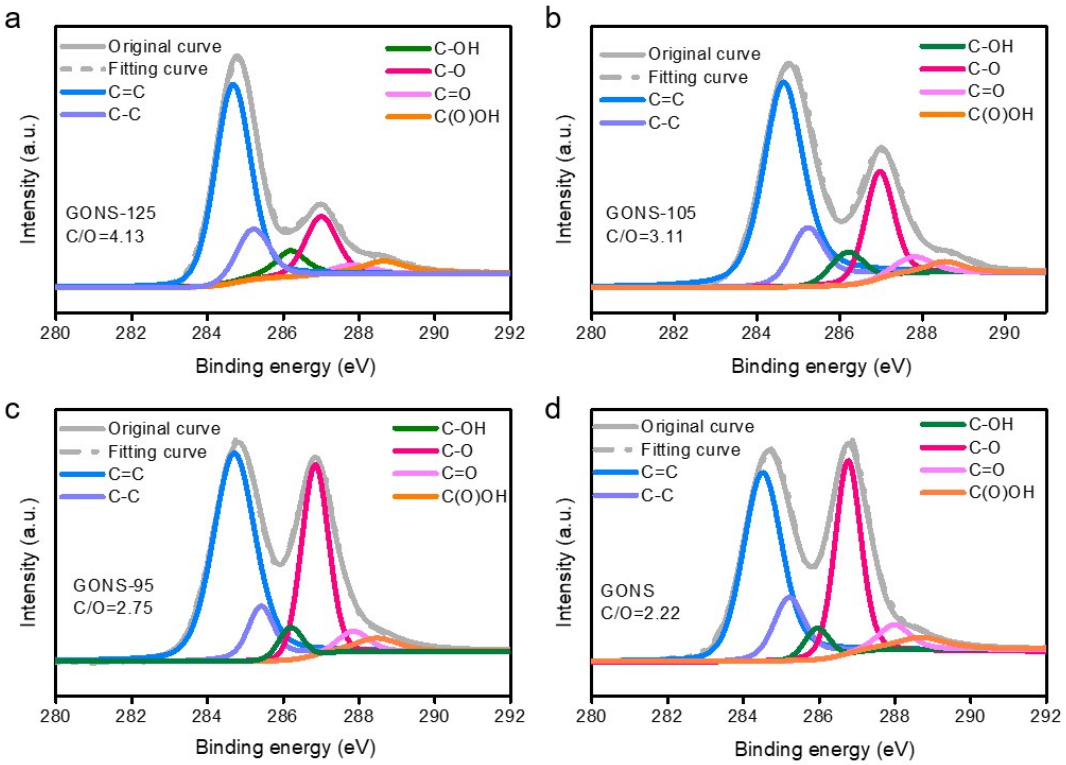

Fig. S21. XPS spectra of C 1s of pristine GONS and differently treated GONS samples with different C/O ratios. (a) GONS-125, (b) GONS-105, (c) GONS-95, (d) pristine GONS Correspondingly, the loading of Mo atoms tended to be positively correlated with the amount of oxygen functional groups.

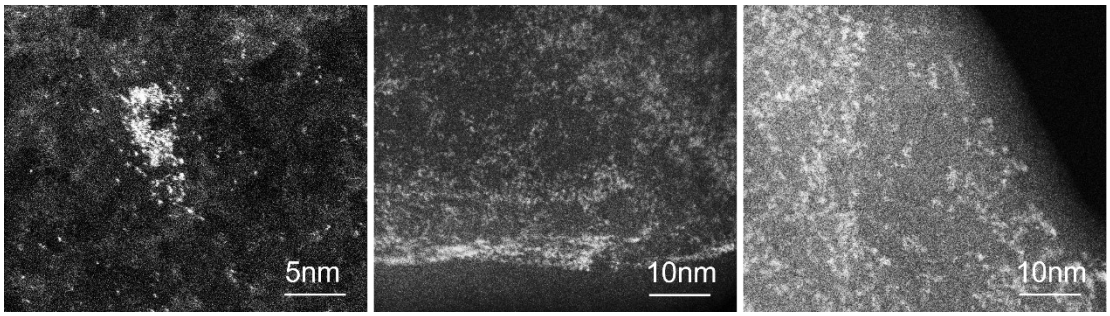

Fig. S22. HAADF-STEM images of Mo-SACs/mrG with triple the amount of metal precursor. It indicates that Mo species tended to be aggregated to form clusters when the amount of $MoCl_5$ precursor is greatly increased to exceed the possible anchoring sites.

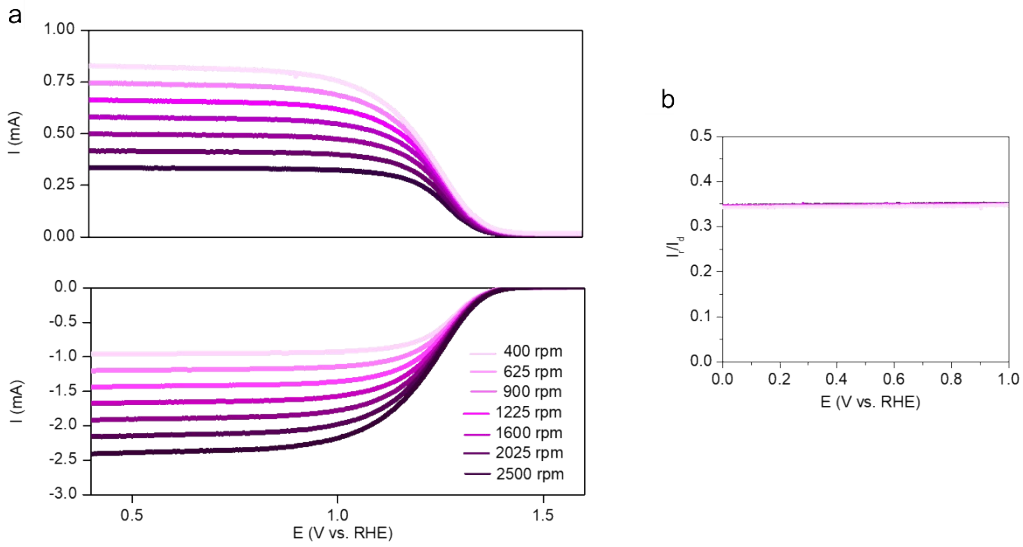

Fig. S23. RRDE collection efficiency calibration. (a) Linear sweep voltammetry curves recorded on a bare glassy carbon rotating disc in 0.1 M Na_2SO_4 supporting electrolyte with 10 mM $K_3Fe(CN)_6$. Sweep rates: 10 mV s^{-1}, E_{ring} = 1.4 V vs. RHE. (b) The ratio of the diffusion-limited current recorded on the disc and ring at different rotating speeds. $N=i_r/i_d=0.347$.

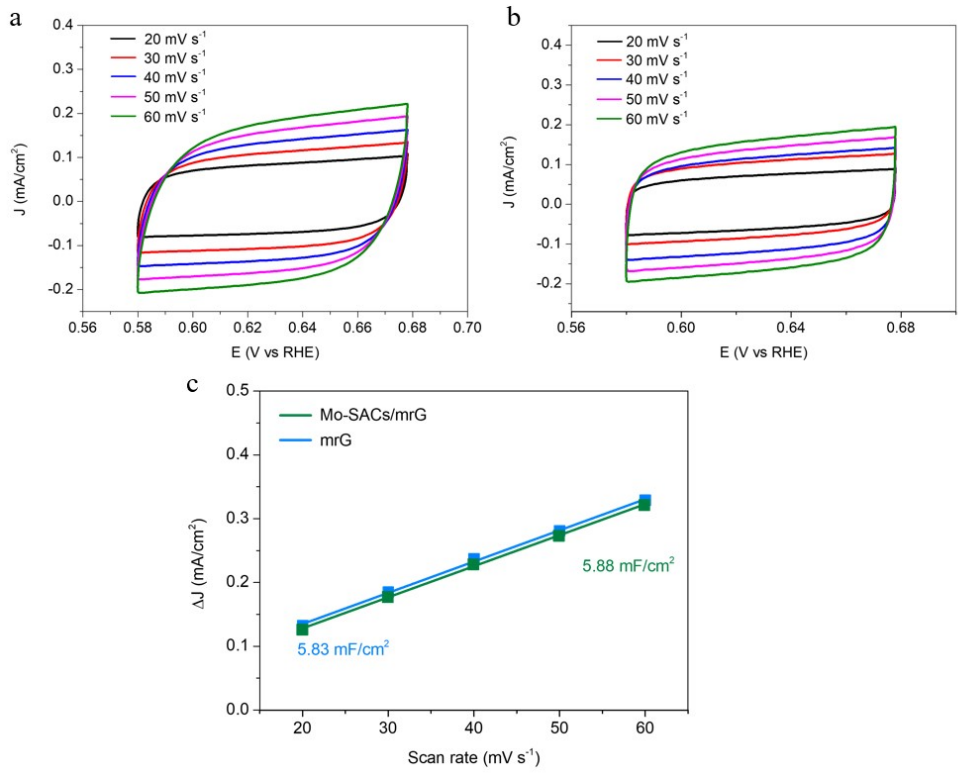

Fig. S24. CV curve of Mo-SACs/mrG (a) and mrG (b) with different scaning rates from 20 to 60 mV s^{-1} at the non-Faradic range. c) normalized current densities of Mo-SACs/mrG and mrG.

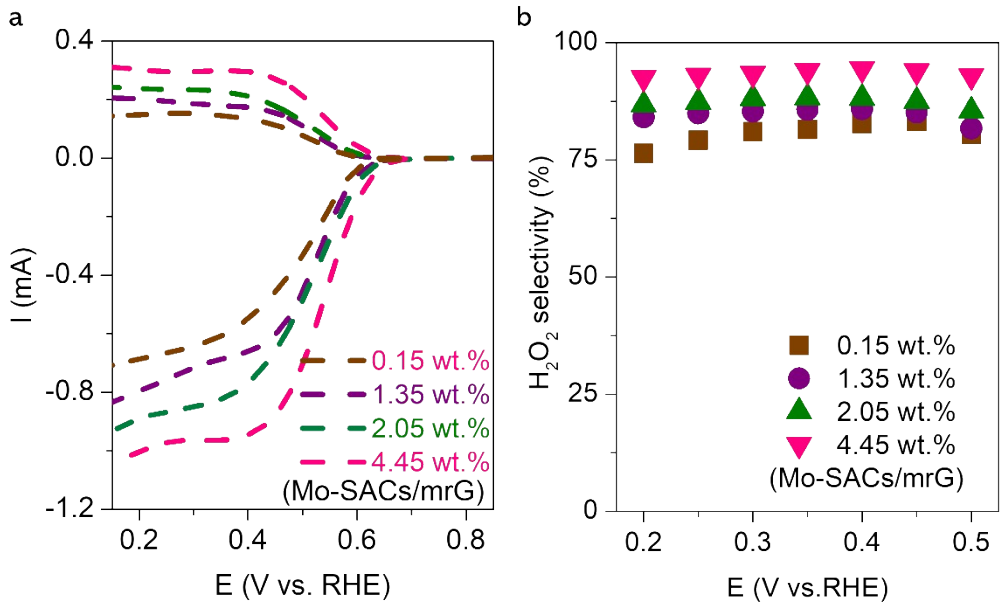

Fig. S25. RRDE curves and selectivity of Mo-SACs/mrG with different loadings. (a) RRDE curves of Mo-SACs/mrG with different loadings. (b) Selectivity of Mo-SACs/mrG with different loadings. The selectivity of H_2O_2 production for the Mo-SACs/mrG exhibits a stepwise increase from 82% to 95% as increasing the Mo content from 0.15 wt.% to 4.45 wt.%.

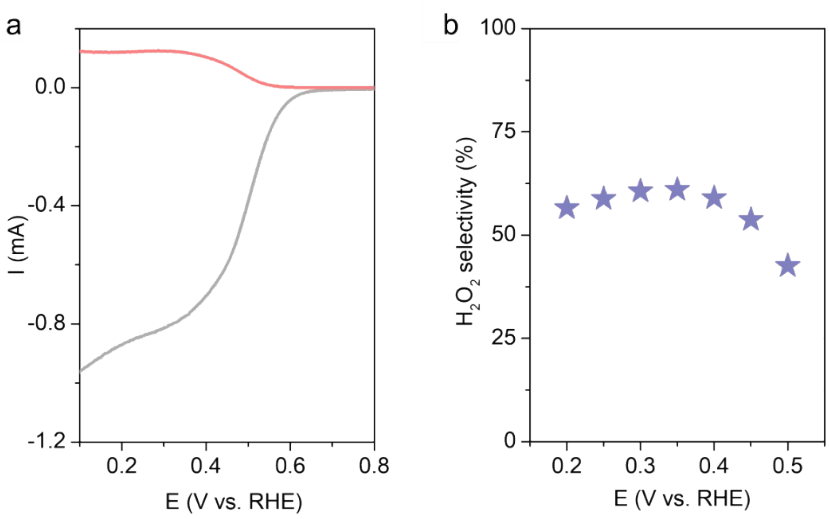

Fig. S26. RRDE curves and selectivity of Mo-cluster/mrG. (a) RRDE curves and (b) selectivity of Mo-cluster/mrG. The selectivity of H_2O_2 production for the Mo-cluster/mrG exhibits a shaprly decrease compared to that of Mo-SACs/mrG.

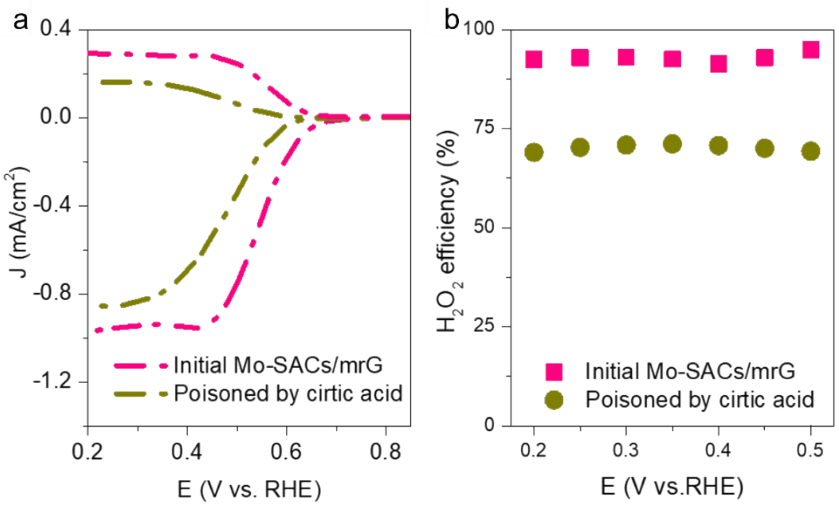

Fig. S27. RRDE curves and selectivity of poisoning test. (a) RRDE curves and (b) selectivity of Mo-SACs/mrG with and without poisoning agent. The poisoning experiment was conducted by adding 0.1 M citric acid in 0.1 M Na_2SO_4 electrolyte since the citric acid can strongly interact with the Mo center.

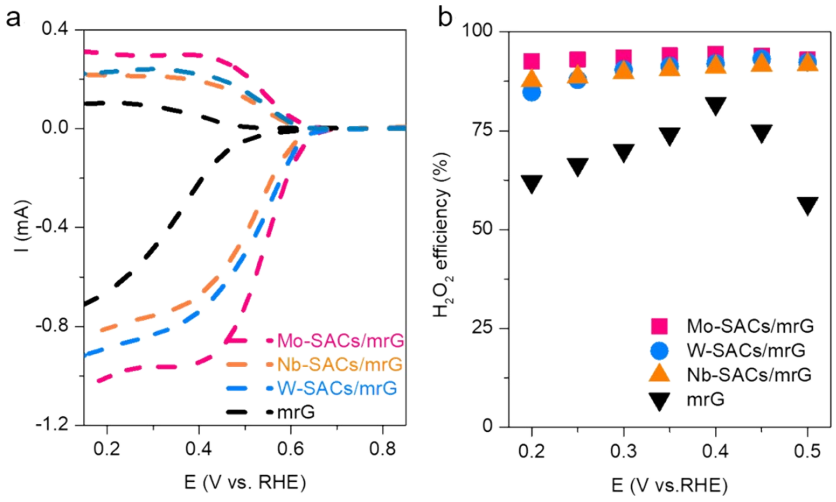

Fig. S28. RRDE curves selectivity of mrG, Nb-SACs/mrG, W-SACs/mrG and Mo-SACs/mrG under 0.1 M Na_2SO_4. (a) RRDE curves of mrG, Nb-SACs/mrG, W-SACs/mrG and Mo-SACs/mrG. (b) Selectivity of mrG, Nb-SACs/mrG, W-SACs/mrG and Mo-SACs/mrG.

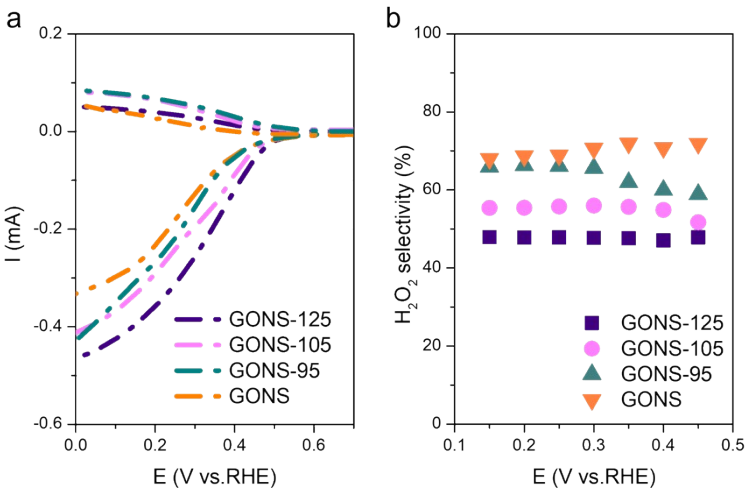

Fig. S29. RRDE curves and H_2O_2 selectivity of pristine GONS and differently treated GONS samples with different C/O ratios. (a) RRDE curves and (b) selectivity of GONS samples.

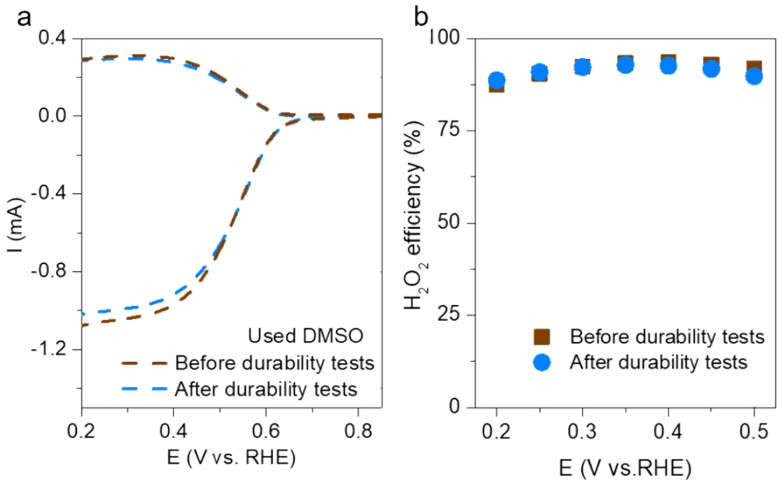

Fig. S30. RRDE curves of Mo-SACs/mrG before/after 7 h durability tests. (a) RRDE curves of Mo-SACs/mrG before/after durability tests. (b) Selectivity of Mo-SACs/mrG before/after durability tests. The negligible difference indicates the high stability of Mo-SACs/mrG.

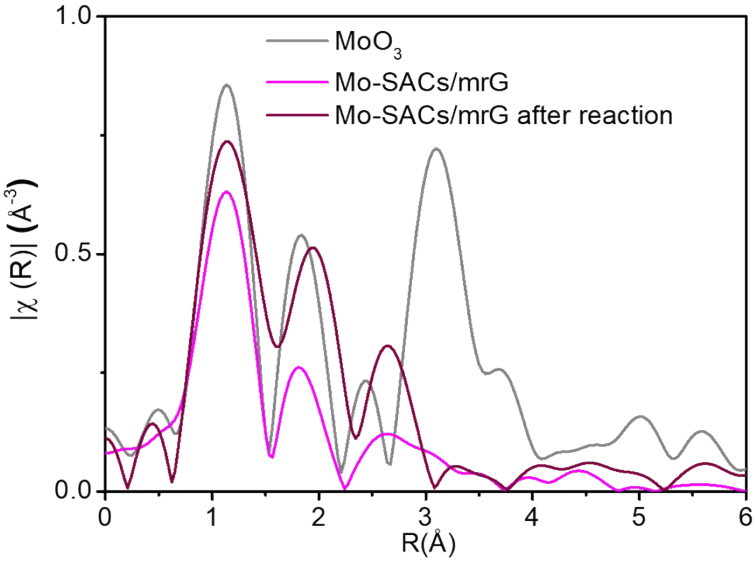

Fig. S31. EXAFS of MoO_3, Mo-SACs/mrG and Mo-SACs/mrG after reaction. No Mo-Mo bond can be detected in the fresh and used Mo-SACs/mrG based on analysis of the EXFAS spectra.

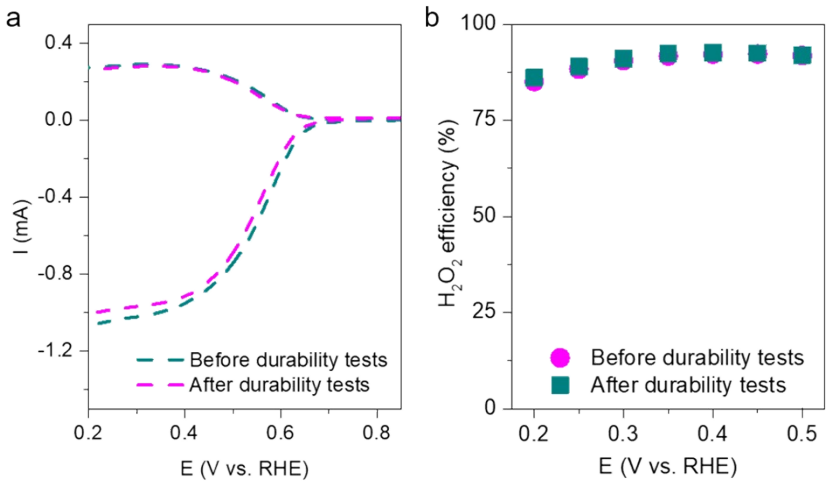

Fig. S32. RRDE curves of Mo-SACs/mrG before/after 7 h durability tests fabricated with the used DMSO. (a) RRDE curves of Mo-SACs/mrG before/after durability tests fabricated with the used DMSO. (b) Selectivity of Mo-SACs/mrG before/after durability tests. The negligible difference indicates the high stability of Mo-SACs/mrG fabricated with the used DMSO.

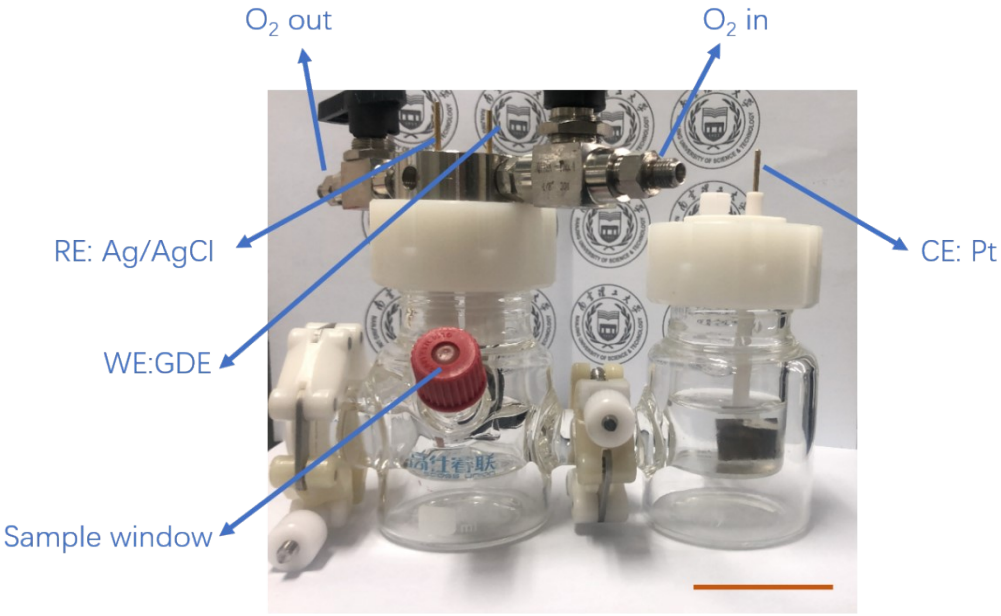

Fig. S33. Optical image of the two-cell device with Mo-SACs/mrG GDE as working electrode, Pt foil as counter electrode and Ag/AgCl electrode as the reference. Scale bar, 5 cm.

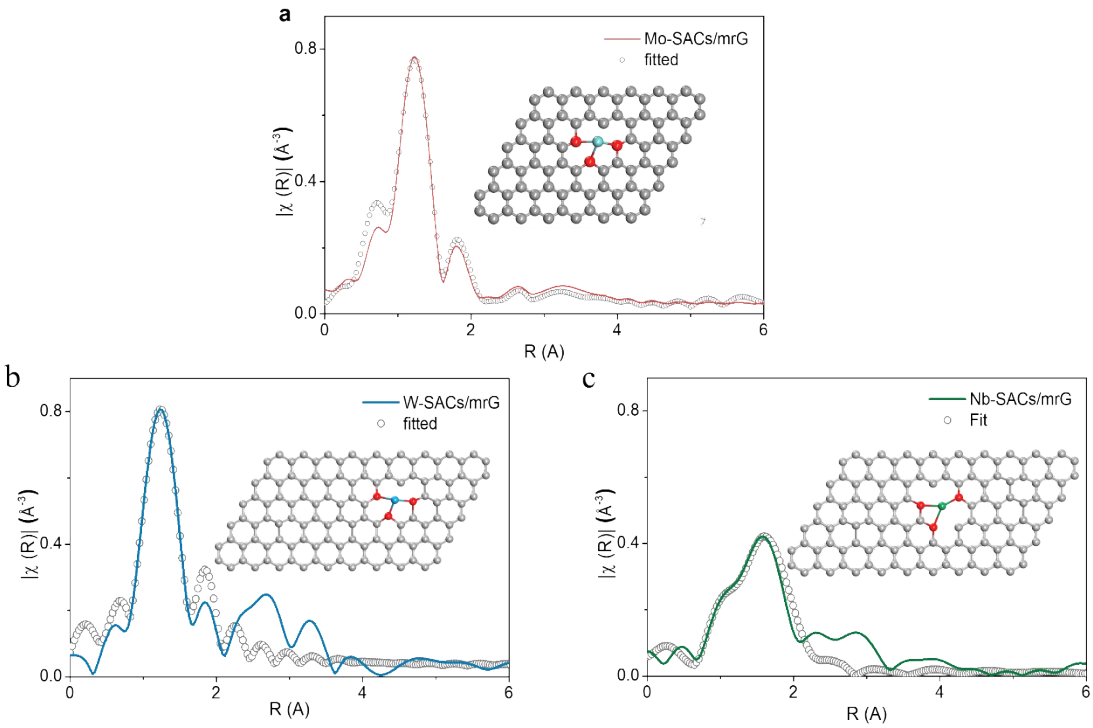

Fig. S34. EXAFS fitting and model structure of with the paths of (a) Mo-O_3-C. (b) W-O_3-C. and (c) Nb-O_3-C.

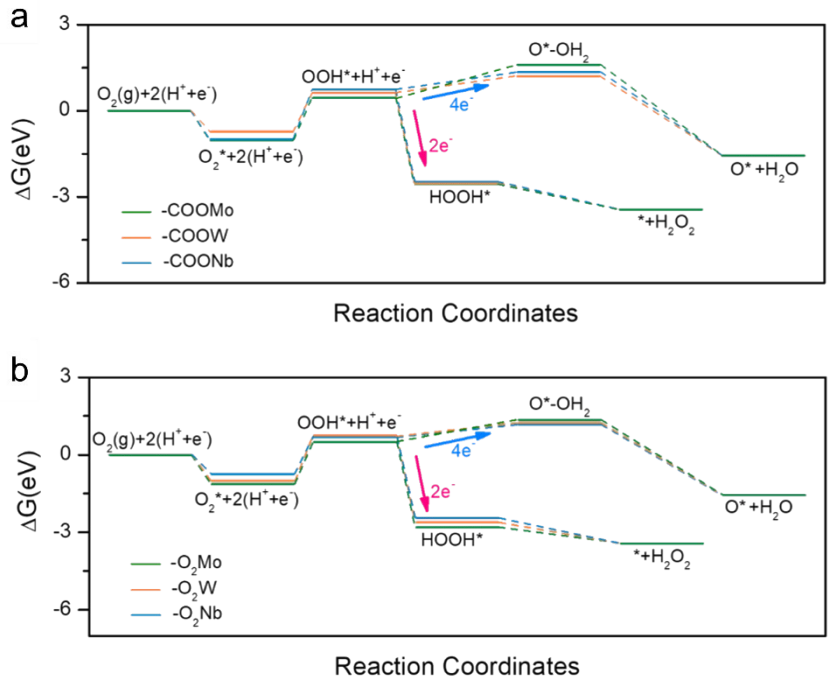

Fig. S35. Free energy of the $2e^-$ and $4e^-$ ORRs for different structures with different metal species. Free energy of the $2e^-$ and $4e^-$ ORRs plotted at U= 0 V and pH=7 for (a) carboxyl structures with different metal species (-OOMo, -OOW and -OONb) and (b) carbonyl structures with different metal species (-NbO_2, -MoO_2 and -WO_2).

Table S1. Summary of the TOFs of various catalysts for electrochemical H_2O_2 production based on the similar active sites number.

Catalyst	Active site	TOF (s^{-1})	Ref
Mo-SACs/mrG (4.45 wt.%)	**Mo**	**7.1**	**This work**
Mo-SACs/mrG (2.05 wt.%)	**Mo**	**5.85**	**This work**
Mo-SACs/mrG (1.35 wt.%)	**Mo**	**4.68**	**This work**
Mo-SACs/mrG (0.15 wt.%)	**Mo**	**4.1**	**This work**
Co1-NG(O)	Co	3.38	34
F-mrG	sp2-hybridized carbon near-ring ether defects	0.088	41
Single atom Pt/HSC	Pt	0.117	19
Single atom Pt/TiN	Pt	0.0789	43
Au-Pt-Ni	Au and Pt	0.0768	44

Table S2. Comparison of fitting results of Mo K-edge EXAFS data in Fig. S9 and theoretical models. σ2 is Debye–Waller factor; E0 is energy shift; R-factor reflects the deviation error of fitting.

Sample	**Path**	**R (Å)**	**σ^2 (Å^2)**	**R-factor (%)**
Mo-SACs/mrG	Mo-O	2.12	0.002	1.3
-O_3Mo	Mo-O	2.11	-	-
-O_2Mo	Mo-O	2.25	-	-
-COOMo	Mo-O	1.92	-	-

References

[1] E. Jung, H. Shin, B. H. Lee, V. Efremov, S. Lee, H. S. Lee, J. Kim, S. Park, K.S.Lee, S. P. Cho, J. S. Yoo, Y. E. Sung, T. Hyeon, Atomic-level tuning of Co–N–C catalyst for high-performance electrochemical H_2O_2 Production, Nat. Mater, 19 (2020) 436-442.

[2] H.W. Kim, M.B. Ross, N. Kornienko, L. Zhang, J. Guo, P. Yang, B.D. McCloskey, Efficient hydrogen peroxide generation using reduced graphene oxide-based oxygen reduction electrocatalysts, Nat. Catal, 1 (2018) 282-290.

[3] C.H. Choi, M. Kim, H.C. Kwon, S. J. Cho, S. Yun, H. T. Kim, K. J. J. Mayrhofer, H. Kim, M. Choi, Tuning selectivity of electrochemical reactions by atomically dispersed platinum catalyst, Nat. Commun., 7 (2016) 10922.

[4] S. Yang, J. Kim, Y. J. Tak, A. Soon, H. Lee, Single-Atom Catalyst of Platinum Supported on Titanium Nitride for SelectiveElectrochemical Reactions, Angew. Chem. Int. Ed., 55 (2016) 2058-2062.

[5] Z. Zheng, Y. H. Ng, D. W. Wang, R. Amal, Epitaxial Growth of Au–Pt–Ni Nanorods for Direct High Selectivity H_2O_2 Production, Adv. Mater, 28 (2016) 9949-9955.